A Cascaded Synchrosqueezing Transform for Precise Analysis of Seismic Signal

Xiaokai Wang, *Member, IEEE*, Dawei Liu, Wenchao Chen, and Chun Li

***Abstract*— Time–frequency (TF) analysis represents a potent tool for processing and interpreting seismic data. Synchrosqueezing transforms (SSTs) remarkably enhance frequency resolution by accumulating coefficients along the frequency axis. However, their TF resolution is related to their mother's TF transforms. The high-order Fourier-based SST (FSST) with a long window exhibits improved frequency resolution, albeit at the cost of mixing detailed frequency variations. Conversely, a high-order FSST with a short window provides enhanced time resolution but suffers from low-frequency resolution and component interference between multiple components of a complex signal. To ameliorate this, our study proposes a cascaded high-order FSST. Our proposed approach commences with a long-window high-order FSST to decompose a complicated signal into multiple components. Subsequently, a short-window high-order FSST is applied to each component. By summing the squeezed TF representations of all components, we generate a TF representation that boasts the improved TF resolution with the cost of involving multiple high-order FSSTs. The visual evaluation and sparsity measure are used to show our method's efficacy and TF resolution over common high-order FSST through a synthetic multicomponent signal (MCS) with two components. The wavelets interference would make the seismic signal's frequency component change. Therefore, further substantiation comes from two wavelet-interference-related examples: the field data example about cycle interbeds and an HST-induced seismic data example, wherein our proposed transform demonstrates its superior ability in precisely tracking subtle frequency variations with time and its advantages over common high-order FSST in extracting cycle thin-interbeds' thickness variation along depth and characterizing the HST speed.**

***Index Terms*— Cascaded synchrosqueezing transform (SST), seismic data analysis, short-time Fourier transform (STFT).**

I. Introduction

SEISMIC signals are commonly represented as the convolution of time-varying wavelets and reflection coefficients, rendering them archetypal time-varying signals. Traditional time-domain and frequency-domain analyses fall short of capturing the concomitant variations in energy distribution across both time and frequency simultaneously. Therefore, they cannot sufficiently analyze this typical time-varying signal. In contrast, time–frequency (TF) analysis can analyze a time-varying signal from the time and frequency domain simultaneously. This advantage has led to its widespread application in seismic signal processing and interpretation. Noteworthy applications include spectral decomposition [1], [2], [3], [4], [5], sequence analysis [6], instantaneous attribute extraction [6], [7], [8], reservoir characterization [9], [10], [11], as well as fault detection [12], [13].

Many TF analyzing methods have been proposed to extract the energy distribution in the TF domain. Short-time Fourier transform (STFT) [14], continuous wavelet transform (CWT) [15], [16], and the Stockwell transform (ST) [17] are the three typical representatives of the linear TF transform. Compared with the STFT's fixed window function, CWT and ST utilize a frequency-varying window function. Thus, CWT and ST have higher frequency resolution and lower time resolution at the low-frequency part, but have lower frequency resolution and higher time resolution at the high-frequency part. These linear TF transforms have a signal reconstruction ability, but suffer from a limited TF resolution due to the uncertainty principle [18]. The Wigner–Ville distribution (WVD) aimed to break the TF resolution limit caused by the uncertainty principle. Although WVD can provide a perfect TF spectrum for some simple signals, it suffers from severe cross-term interference [19]. The Cohen class TF distribution smoothens the WVD to suppress the cross-term interference but bears some disadvantages, such as negative values, cross-term interference, the loss of TF resolution, and irreversibility [20]. Although the spectrum reassignment can sharpen the TF spectrum by accumulating each TF point's energy to its gravity center [21], [22], it cannot be used to reconstruct the signal.

Many signals in the real world can be modeled as a superposition of some amplitude-modulated and frequency-modulated (AM–FM) components. Therefore, they are called multicomponent signals (MCSs). Newly developed synchrosqueezing transforms (SSTs), which are based on some commonly used linear TF representations, such as STFT, CWT, and ST [4], [23], [24], [25], have been designed to deal with the MCS. They can improve the TF resolution by moving the TF coefficients along the frequency direction and can be used to reconstruct the signal spontaneously. These common SSTs can generate a perfect TF spectrum for the MCS with sinusoidal components. To deal with the MCS with linear FM components, second-order SSTs have been proposed to further improve the TF spectra's concentrations [26], [27], [28], [29]. To achieve a concentrated time-frequency representation

Manuscript received 14 August 2023; revised 24 November 2023; accepted 8 December 2023. Date of publication 12 December 2023; date of current version 17 January 2024. This work was supported by the National Natural Science Foundation of China under Grant 41974131, Grant 42374135, and Grant 41774135. *(Corresponding author: Wenchao Chen.)*

The authors are with the School of Information and Communication Engineering, Xi'an Jiaotong University, Xi'an, Shaanxi 710049, China (e-mail: xkwang@xjtu.edu.cn; liudawei2015@stu.xjtu.edu.cn; wencchen@xjtu.edu.cn; lichun2019@stu.xjtu.edu.cn).

Digital Object Identifier 10.1109/TGRS.2023.3341793

(TFR) for an MCS with quadratic or cubic FM components, SST has been extended to high-order SST [30], [31]. Because the SSTs can provide a concentrated TF representation, they have been extensively used in seismic data processing and interpretation like noise attenuation [32], [33], [34], [35], [36], spectrum decomposition [37], [38], [39], [40], [41], [42], [43], [44], seismic data interpretation [2], [4], [28], [45], [46], [47], gas reservoir identification [9], [25], [48], [49], seismic data modal separation [50], [51], quality factor estimation [52], phase compensation [53], [54], inversion [55], coherence extraction [56], and reservoir characterization [57], [58].

Many SSTs, such as STFT-, CWT-, and ST-based SST, have been successfully used to obtain the high-TF resolution spectra for the MCS. However, because they only move TF coefficients along the frequency or time direction, they may not track each component's slight frequency variation along time for an MCS. In this study, we mainly focus on the Fourier-based SST (FSST), which has a fixed TF resolution in the entire TF domain and try to improve it. Although the Nth order FSST (FSSTN) [30] can produce a more concentrated TF spectrum than STFT and other lower order FSSTs, it still suffers from some problems. Suppose there is one MCS that contains two slanted FM components whose instantaneous frequency (IF) has a small periodic fluctuation. Besides, the frequency interval between two components is minimal. The FSST4 of this MCS suffers from low time resolution or component interference. Fig. 1(a) and (b) shows this MCS's two TF spectra based on STFT and FSST4 with a long Gaussian window function. The long window STFT [Fig. 1(a)] mixes the frequency variation. Therefore, although long window FSST4 [Fig. 1(b)] can provide a very concentrated TF spectrum to depict two components' approximate frequency variation trend, it could not track the ideal frequency variations, which are indicated by two blue curves in Fig. 1(b). That is to say, the long window STFT and FSST suffer from low time resolution. The middle window STFT [Fig. 1(c)] still cannot reflect these two components' frequency variations, but it appears that the two components are not purely linear chirps. Although the middle window FSST4 [Fig. 1(d)] can provide a more concentrated TF spectrum, it cannot track the ideal frequency variation. In addition, FSST4 with a middle window suffers from little interference between the two components. The small window STFT [Fig. 1(e)] and corresponding FSST4 [Fig. 1(f)] can show the frequency variation over temporal direction but are strongly affected by the two components' interference. Therefore, the small window FSST4 does not concentrate near the ideal frequency curves [Fig. 1(f)]. In summary, although the high-order FSST can gain an ideal TF performance for one component signal, it still cannot balance the time resolution and the component interference.

Therefore, this study simultaneously enhances the time resolution and reduces component interference in high-order FSST, proposing a cascaded FSST approach for precise seismic signal analysis. This study is organized as follows. Section II introduces the theoretical principles of FSSTN and the proposed cascaded FSST. Section III demonstrates a synthetic data example to demonstrate the proposed transform's advantages over the commonly used high-order FSST. In addition, one oilfield data example and one high-speed train (HST)-induced seismic data example are utilized to illustrate the proposed method's precision. Some conclusions are drawn in Section IV.

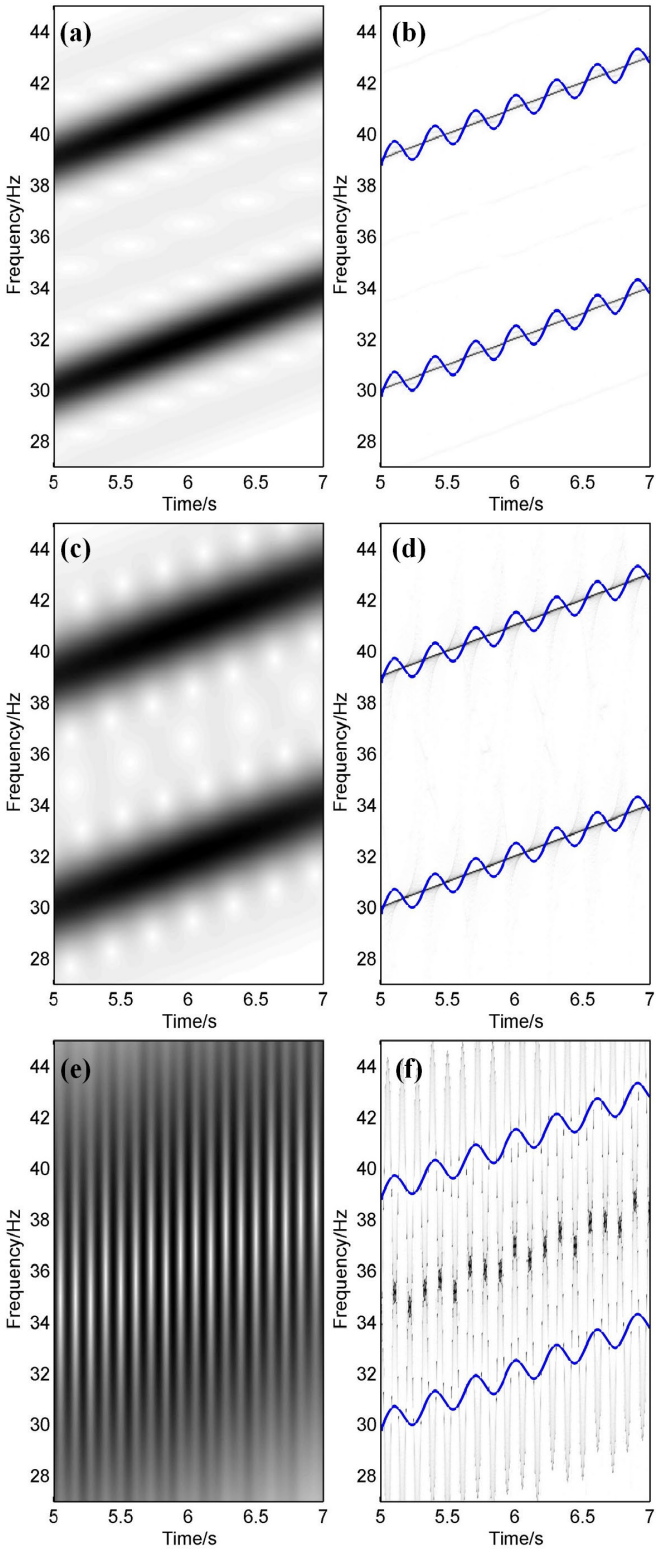

Fig. 1. TF spectra of one synthetic MCS with two slanted FM components. (a) STFT and (b) FSST4 with a long Gaussian window ($\sigma = 0.275$). (c) STFT and (d) FSST4 with a middle Gaussian window ($\sigma = 0.15$). (e) STFT and (f) FSST4 with a short Gaussian window ($\sigma = 0.03$). The blue curves show the ideal instantaneous frequencies of two FM components.

II. Method

A. Short-Time Fourier Transform (STFT)

Let $g(t)$ be an even, real-valued window function with a unit norm. The STFT of the signal $x(t)$ with respect to the window function $g(t)$ can be defined by

$$V_g(t,\omega) = \int_R x(\tau)\overline{g(\tau-t)}e^{-j\omega(\tau-t)}d\tau = \int_R x(\tau+t)\overline{g(\tau)}e^{-j\omega\tau}d\tau \quad (1)$$

where $g(t)$ represents a window function, and $\overline{g(t)}$ represents the conjugate of $g(t)$. The STFT definition in (1) differs from the usual definition by a factor $e^{-j\omega t}$. Meanwhile, the STFT in (1) can be realized in the frequency domain as follows:

$$V_g(t,\omega) = \frac{1}{2\pi}\int_R X(\omega_1)\overline{G(\omega_1-\omega)}e^{-j\omega_1 t}d\omega_1 \quad (2)$$

where $X(\omega)$ and $G(\omega)$ represent the Fourier transforms of signal $x(t)$ and window function $g(t)$, respectively. The signal can then be reconstructed by using either of the following methods:

$$x(t) = \frac{1}{2\pi}\iint V_g(t,\omega)g(t-t_1)e^{j\omega(t-t_1)}dt_1 d\omega \quad (3)$$

or

$$x(t) = \frac{1}{2\pi g(0)}\int_R V_g(t,\omega)d\omega. \quad (4)$$

The second reconstruction in (4) is frequently adopted due to its high efficiency compared with the method in (3). In addition, the integration range in (3) and (4) can be restricted to a small area to reconstruct the interested part. However, we must mention that the TF resolution of the STFT cannot overcome the restriction caused by the Heisenberg uncertainty [18].

B. MCS Model

A real signal can be converted to a complex signal via the Hilbert transform. If we let $A(t)$ and $\phi(t)$ be the instantaneous amplitude (IA) and instantaneous phase (IP), respectively, and let $A(t)$ and IF $\phi'(t)$ be positive and slowly varying, then the oscillating function $x(t) = A(t)e^{j\phi(t)}$ is one AM–FM mode. The IA and IF can be easily approximated in the vicinity of a fixed time. A first-order expansion of phase $\phi(t)$ and a zeroth-order expansion of $A(t)$ can lead to an approximation of $x(\tau)$ near t

$$x_t(\tau) \approx A(t)e^{j[\phi(t)+\phi'(t)(\tau-t)]} \quad (5)$$

where τ is a time that is close to the fixed time t. The STFT of $x(t)$ can be approximated via the STFT of $x_t(\tau)$ [24]

$$V_g(t,\omega) \approx x(t)G(\omega-\phi'(t)). \quad (6)$$

The expression in (6) proves that the support region of $V_g(t,\omega)$ is restricted to one TF strip that is centered on the ridge corresponding to the IF $\phi'(t)$, with the width of the TF strip dependent on the width of $G(\omega)$.

The MCS can be defined as the superposition of M AM–FM components

$$x(t) = \sum_{m=1}^{M} x_m(t) = \sum_{m=1}^{M} A_m(t)e^{j\phi_m(t)} \quad (7)$$

where $x_m(t)$ satisfies $\phi_1'(t) < \phi_2'(t) < \cdots < \phi_M'(t)$. Each mode can be distinguished and retrieved via the STFT of $x(t)$ when the distance between two ridges is larger than the width of $G(\omega)$.

C. Nth-Order STFT-Based SST (FSSTN)

Suppose we have a component $x(t) = e^{A(t)+j\phi(t)}$, where $A(t)$ and $\phi(t)$ are two Nth-order polynomials, and the Nth-order Taylor expansions of $A(t)$ and $\phi(t)$ at time t can be expressed as follows:

$$A(\tau+t) = \sum_{k=0}^{K}\frac{A^{(k)}(t)}{k!}\tau^k \quad (8)$$

$$\phi(\tau+t) = \sum_{k=0}^{K}\frac{\phi^{(k)}(t)}{k!}\tau^k \quad (9)$$

where $A^{(k)}(t)$ and $\phi^{(k)}(t)$ denote the kth derivatives of $A(t)$ and $\phi(t)$ at time t. The AM–FM component $x(\tau)$ has an expansion at time t

$$x(\tau+t) = \exp\left\{\sum_{k=0}^{K}\frac{A^{(k)}(t)+j\phi^{(k)}(t)}{k!}\tau^k\right\}. \quad (10)$$

After replacing the $x(\tau+t)$ in (1) with (10), the STFT of $x(\tau)$ can be reformulated as follows:

$$V_g(t,\omega) = \int_R exp\left\{\sum_{k=0}^{K}\frac{A^{(k)}(t)+j\phi^{(k)}(t)}{k!}\tau^k\right\}\overline{g(\tau)}e^{-j\omega\tau}d\tau. \quad (11)$$

By taking the partial derivative of $V_g(t,\omega)$ for t, (11) can be changed to

$$\partial_t V_g(t,\omega) = \sum_{k=1}^{K}\frac{A^{(k)}(t)+j\phi^{(k)}(t)}{(k-1)!}V_{t^{k-1}g}(t,\omega) \quad (12)$$

where $V_{t^{k-1}g}(t,\omega)$ is a signal's STFT with the window function $t^{k-1}g(t)$. The local complex IF $\hat{\omega}(t,\omega)$ can be estimated by dividing by $\partial_t V_g(t,\omega)$ with $jV_g(t,\omega)$

$$\hat{\omega}(t,\omega) = \frac{\partial_t V_g(t,\omega)}{jV_g(t,\omega)} = -jA'(t)+\phi'(t)+\sum_{k=2}^{K}q^{[k,K]}(t)\frac{V_{t^{k-1}g}(t,\omega)}{V_g(t,\omega)} \quad (13)$$

where

$$q^{[k,K]}(t) = \frac{A^{(k)}(t)-j\phi^{(k)}(t)}{(k-1)!} \quad (14)$$

where $\phi'(t)$ in (13) is the actual IF for $x(t)$. Therefore, one critical step in FSSTN is to estimate $\phi'(t)$.

1) First-Order FSST: If $A(t)$ and $\phi(t)$ are two first-order polynomials, (13) can be simplified to

$$\hat{\omega}(t,\omega) = -jA'(t) + \phi'(t). \tag{15}$$

Then, the actual IF $\phi'(t)$ can be estimated by the real part of $\hat{\omega}(t,\omega)$

$$\hat{\omega}^{[1]}(t,\omega) = \phi^{'}(t) = \mathrm{Re}\left[\hat{\omega}(t,\omega)\right] = \mathrm{Re}\left[\frac{\partial_t V_g(t,\omega)}{jV_g(t,\omega)}\right] \tag{16}$$

where $\mathrm{Re}(z)$ represents extracting the real part of a complex number z. Then, the first-order FSST $\mathrm{FSST}(t,\omega)$ of component $x(t)$ can be obtained by accumulating the STFT coefficient in (t,ω) to a new position $(t,\hat{\omega}^{[1]}(t,\omega))$

$$\mathrm{FSST}(t,\omega) = \int_R V_g(t,\omega_1)\delta\left[\omega - \hat{\omega}^{[1]}(t,\omega_1)\right]d\omega_1 \tag{17}$$

where $\delta(\omega)$ represents the Dirac delta function.

2) Second-Order FSST (FSST2): If $A(t)$ and $\phi(t)$ are two second-order polynomials, (13) can be simplified to

$$\hat{\omega}(t,\omega) = -jA'(t) + \phi'(t) + q^{[2,2]}(t)X_{2,1}(t,\omega) \tag{18}$$

where

$$X_{2,1}(t,\omega) = \frac{V_{tg}(t,\omega)}{V_g(t,\omega)}. \tag{19}$$

To estimate the IF $\phi'(t)$ in (18), we must know $q^{[2,2]}(t)$. By taking the partial derivative of the left and right terms in (18) for ω, one estimation of $q^{[2,2]}(t)$ can be calculated by

$$\hat{q}^{[2,2]}(t,\omega) = \frac{\partial_\omega\hat{\omega}(t,\omega)}{\partial_\omega X_{2,1}(t,\omega)}. \tag{20}$$

Then, the actual IF $\phi'(t)$ can be estimated by

$$\hat{\omega}^{[2]}(t,\omega) = \mathrm{real}\left[\hat{\omega}(t,\omega) - \hat{q}^{[2,2]}(t,\omega)X_{2,1}(t,\omega)\right]. \tag{21}$$

Then, second-order FSST $\mathrm{FSST2}(t,\omega)$ of component $x(t)$ can be obtained by accumulating the STFT coefficient in (t,ω) to a new position $(t,\hat{\omega}^{[2]}(t,\omega))$

$$\mathrm{FSST2}(t,\omega) = \int_R V_g(t,\omega_1)\delta\left[\omega - \hat{\omega}^{[2]}(t,\omega_1)\right]d\omega_1. \tag{22}$$

3) Third-Order FSST (FSST3): If $A(t)$ and $\phi(t)$ are the two three-order polynomials, (13) can be simplified to

$$\hat{\omega}(t,\omega) = -jA'(t) + \phi'(t) + \sum_{k=2}^{3} q^{[k,3]}(t)X_{k,1}(t,\omega) \tag{23}$$

where

$$X_{k,1}(t,\omega) = \frac{V_{t^{k-1}g}(t,\omega)}{V_g(t,\omega)}. \tag{24}$$

To estimate the IF $\phi'(t)$ in (23), we must know $q^{[2,3]}(t)$ and $q^{[3,3]}(t)$. By taking the partial derivative of the left and right terms in (23) for ω, (23) can be changed to

$$\partial_\omega\hat{\omega}(t,\omega) = q^{[2,3]}(t)\partial_\omega X_{2,1}(t,\omega) + q^{[3,3]}(t)\partial_\omega X_{3,1}(t,\omega). \tag{25}$$

Equation (25) can be simplified to

$$Y_1(t,\omega) = q^{[2,3]}(t) + q^{[3,3]}(t)X_{3,2}(t,\omega) \tag{26}$$

where

$$Y_1(t,\omega) = \frac{\partial_\omega\hat{\omega}(t,\omega)}{\partial_\omega X_{2,1}(t,\omega)} \tag{27}$$

$$X_{3,2}(t,\omega) = \frac{\partial_\omega X_{3,1}(t,\omega)}{\partial_\omega X_{2,1}(t,\omega)}. \tag{28}$$

One estimation of $q^{[3,3]}(t)$ can be estimated by computing the partial derivative of the left and right terms in (26) for ω again

$$\hat{q}^{[3,3]}(t,\omega) = \frac{\partial_\omega Y_1(t,\omega)}{\partial_\omega X_{3,2}(t,\omega)}. \tag{29}$$

By replacing $\hat{q}^{[3,3]}(t,\omega)$ in (26) with (29), $q^{[2,3]}(t)$ can be estimated by

$$\hat{q}^{[2,3]}(t,\omega) = Y_1(t,\omega) - \hat{q}^{[3,3]}(t,\omega)X_{3,2}(t,\omega). \tag{30}$$

After obtaining the estimations of $q^{[2,3]}(t)$ and $q^{[3,3]}(t)$, the actual IF $\phi'(t)$ can be estimated by

$$\hat{\omega}^{[3]}(t,\omega) = \mathrm{real}\left[\hat{\omega}(t,\omega) - \hat{q}^{[2,3]}(t,\omega)X_{2,1}(t,\omega) - \hat{q}^{[3,3]}(t,\omega)X_{3,1}(t,\omega)\right]. \tag{31}$$

Then, third-order FSST $\mathrm{FSST3}(t,\omega)$ of component $x(t)$ can be obtained by accumulating the STFT coefficient in (t,ω) to a new position $(t,\hat{\omega}^{[3]}(t,\omega))$

$$\mathrm{FSST3}(t,\omega) = \int_R V_g(t,\omega_1)\delta\left[\omega - \hat{\omega}^{[3]}(t,\omega_1)\right]d\omega_1. \tag{32}$$

Similarly, the fourth-order FSST (FSST4) and higher order FSST can be computed with the same but more complicated iterative procedure. Furthermore, all FFSTNs can be used to reconstruct the signal by replacing $V_g(t,\omega)$ in (4) with FSSTN.

D. Cascaded FSSTN

Although the long window high-order FSST has good frequency resolution in the TF domain, it mixes the detailed frequency variation for a complicated FM component [as shown in Fig. 1(a) and (b). Therefore, the long window high-order FSST suffers from a low time resolution in the TF domain. The short-window STFT and short-window high-order FSST have good time resolution but suffer from low frequency resolution and component interference for an MCS [as shown in Fig. 1(e) and (f). Here, a cascaded high-order FSST is proposed to improve the low time resolution for long window high-order FSST and components interference for short window high-order FSST.

Here, the Gaussian function is used as a window function for STFT and FSSTN. The long window high-order FSST has good frequency resolution. Therefore, we utilize long window high-order FSSTN to an MCS $x(t)$ and denote it as $\mathrm{FSSTN}(x,\sigma;t,\omega)$, where σ is the standard deviation controlling the Gaussian window's width.

To evaluate different TF spectra's resolution quantitatively, a sparsity measure based on accumulation is used. We reshape 2-D TF spectra to 1-D dataset and sort the 1-D dataset's squares in descending order. The reordering coefficients' square is denoted by $\mathrm{RC}[n]$. Assume that N is the number of coefficients. We accumulate the $\mathrm{RC}[n]$

$$\mathrm{ACCU}[m] = \sum_{n=1}^{m}\mathrm{RC}[n] \tag{33}$$

until we find a count M who satisfies

$$\mathrm{ACCU}[M-1]=\sum_{n=1}^{M-1}\mathrm{RC}[n]<0.99*\mathrm{ACCU}[N] \quad (34)$$

and

$$\mathrm{ACCU}[M]=\sum_{n=1}^{M}\mathrm{RC}[n]\geq 0.99*\mathrm{ACCU}[N]. \quad (35)$$

Then, the sparsity measure of FSSTN$(x,\sigma;t,\omega)$ can be defined as the ratio between M and N, and represented by SPAR[FSSTN(x,σ)]. The concentrated TF spectra would generate a sparsity measure approaching 0.

To get a TF spectrum with high concentration, the sparsity measure of high-order FSST spectra with different σ can be utilized to select the optimal standard deviation $\sigma_{\mathrm{opt}i}$

$$\sigma_{\mathrm{opt}i}=\min_{\sigma}\{\mathrm{SPAR}[\mathrm{FSSTN}(x,\sigma)]\}. \quad (36)$$

Usually, selecting the optimal $\sigma_{\mathrm{opt}i}$ need to compute a series of FSSTNs with different standard deviations, which causes an extensive computational cost. An alternative optimizing method is to use the conjugate gradient algorithm to search for the optimal $\sigma_{\mathrm{opt}i}$ [59].

FSST4 can track the frequency variation for a complicated component than other lower order FSST. Thus, FSST4 is always adopted. After getting a concentrated TF representation FSST4$(x,\sigma_{\mathrm{opt}i};t,\omega)$, the TF plane can be divided into several interesting parts according to each component's ridge [60] or other criteria. Suppose the TF plane $D_{\mathrm{T-F}}$ is divided to K parts and the kth part is represented as D_k, then these K parts should satisfy

$$\bigcup_{k}D_k=D_{\mathrm{T-F}} \quad (37)$$

and

$$D_m\cap D_n=\emptyset,\quad m,n\in\{1,2,\ldots,K\}\text{ and }m\neq n. \quad (38)$$

The FSST4$(x,\sigma_{\mathrm{opt}i};t,\omega)$ within D_k can reconstruct the kth component $\hat{x}_k(t)$

$$\hat{x}_k(t)=\iint_{D_k}\mathrm{FSST4}\big(x,\sigma_{\mathrm{opt}i};t,\omega\big)d\omega. \quad (39)$$

In addition, the reconstruction in (39) can be limited to the interested TF area to obtain the interested component.

Once we obtain several isolated components or the interested components, the component interference in TF analyzing can be improved. The small window high-order FSST has a lower frequency resolution and higher time resolution, but it still can be used for the isolated component to obtain the high TF representation because each component can be reconstructed. Then, an MCS' TF representation with a high time and frequency resolution simultaneously can be obtained. For the kth reconstructed component $\hat{x}_k(t)$, the small window FSST4 can be applied and generates a TF representation FSST4$(\hat{x}_k,\sigma_{\mathrm{small}};t,\omega)$. An MCS' final TF representation $\mathrm{FSST4}_{\mathrm{final}}(t,\omega)$ can be obtained by summing all FSST4$(\hat{x}_k,\sigma_{\mathrm{small}};t,\omega)$

$$\mathrm{FSST4}_{\mathrm{final}}(t,\omega)=\sum_{k=1}^{K}\mathrm{FSST4}\big(\hat{x}_k,\sigma_{\mathrm{small}};t,\omega\big). \quad (40)$$

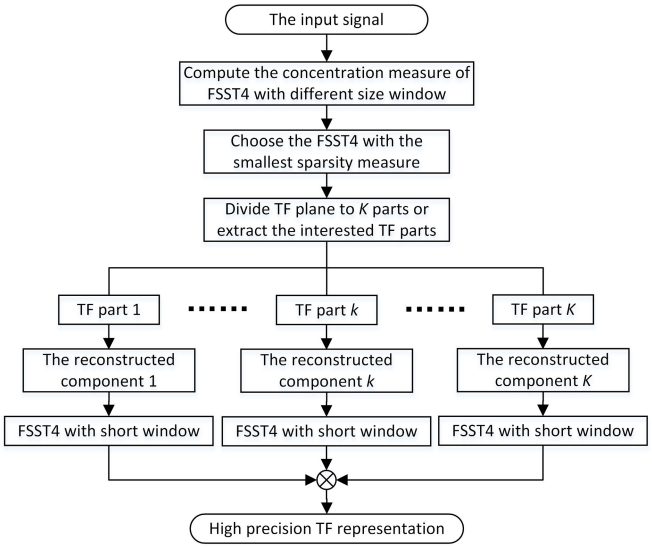

Fig. 2. Proposed method's flowchart.

Because $\{D_1,D_2,\ldots,D_K\}$ can constitute one partition for the TF domain, and each FSST4 is one TF transform, the $\mathrm{FSST4}_{\mathrm{final}}(t,\omega)$ can be considered as one TF representation of $x(t)$. Because $K+1$ FSST4 is used in the Cascaded FSST, the computational cost would increase. The cascaded FSST can be summarized in Fig. 2 with the following steps.

1) Compute the signal's FSST4 with some Gaussian windows with different standard deviations.
2) Using the FSST4's TF sparsity measure to select one optimal standard deviation $\sigma_{\mathrm{opt}i}$ which can generate the smallest TF sparsity measure.
3) Compute the FSST4$(x,\sigma_{\mathrm{opt}i};t,\omega)$ with the optimal standard deviation $\sigma_{\mathrm{opt}i}$.
4) Divide the TF plane into K parts or select the interested TF area.
5) Each component (or the interested components) can be reconstructed by FSST4$(x,\sigma_{\mathrm{opt}i};t,\omega)$ within each TF part (or the interested TF areas).
6) Compute the FSST4 of each reconstructed component with the short window that minimizes the sparsity measure.
7) Sum all components' FSST4 TF representation to generate a high-precision TF representation.

III. Data Examples

A. Synthetic MCS Example

We generated an MCS consisting of two components

$$x(t)=x_1(t)+x_2(t) \quad (41)$$

where

$$x_1(t)=e^{-0.25*(t-5)^2}e^{j2\pi\left\{20t+t^2+\frac{3}{40\pi}\sin\left[\frac{20\pi}{3}(t-5)\right]\right\}} \quad (42)$$

$$x_2(t)=e^{-0.25*(t-5)^2}e^{j2\pi\left\{29t+t^2+\frac{3}{40\pi}sin\left[\frac{20\pi}{3}(t-5)\right]\right\}}. \quad (43)$$

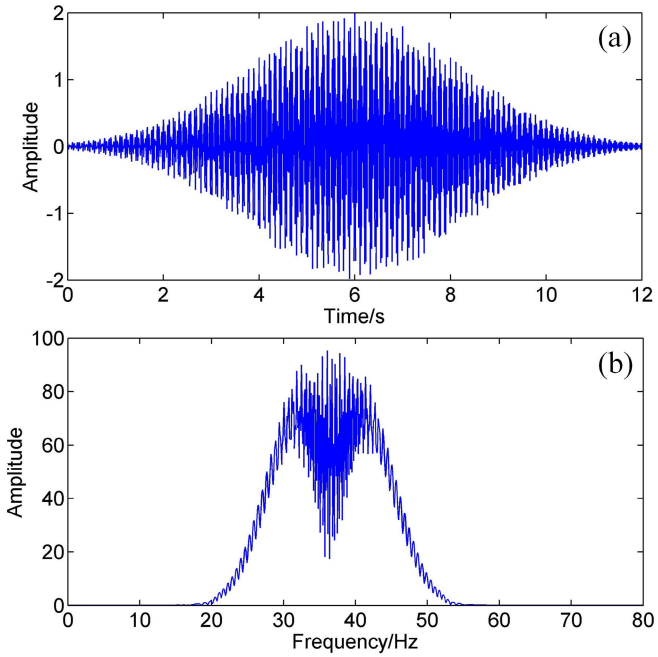

Fig. 3. Synthetic MCS. (a) Waveform. (b) Amplitude spectrum.

The IFs of $x_1(t)$ and $x_2(t)$ are as follows:

$$\mathrm{IF}_1(t) = 20 + 2t + 0.5 \times \cos\left[\frac{20\pi}{3}(t-5)\right] \tag{44}$$

$$\mathrm{IF}_2(t) = 29 + 2t + 0.5 \times \cos\left[\frac{20\pi}{3}(t-5)\right]. \tag{45}$$

These two IFs have a period of 0.3-s fluctuation. In addition, the interval between these two IFs is 9 Hz, which is very small. The waveform and amplitude spectrum of this MCS are shown in Fig. 3(a) and (b). The IFs of two components cannot be observed in the time or the frequency domain. The FSST4 TF spectra with a long Gaussian window ($\sigma = 0.275$), a middle Gaussian window ($\sigma = 0.15$), and a short Gaussian window ($\sigma = 0.03$) are computed, and their zoomed TF spectra have been shown in Fig. 1(b), (d), and (f). Two components' IFs cannot be tracked by these three TF spectra in Fig. 1(b), (d), and (f).

The proposed cascaded FSST is applied to this MCS. A series of Gaussian windows with different standard deviations are utilized in computing the FSST4 of this synthetic MCS. The sparsity measure of FSST4 versus standard deviation is plotted in Fig. 4. We can find that the smallest measure's position is $\sigma = 0.275$. Then, the FSST4 with window size ($\sigma = 0.275$) of the MCS is calculated and shown in Fig. 5. Two ridges can be observed. The TF plane can be divided into two parts (shown in Fig. 5 with red polygon and blue polygon), and two components can be reconstructed.

For each reconstructed component, we compute the FSST4 with a series of Gaussian windows with different standard deviations. The sparsity measure of FSST4 versus standard deviation curves for two reconstructed components are plotted in Fig. 6(a) and (b). $\sigma = 0.03$ can make two curves in Fig. 6 have the smallest measure. Thus, we apply FSST4 with a small Gaussian window ($\sigma = 0.03$) to two reconstructed components and obtain two TF representations [two corresponding TF spectra are shown in Fig. 7(a) and (b)]. By summing these two TF representations, we obtain the final TF representation and show the zoomed TF spectra in Fig. 7(c). As a comparison, two ideal IFs are shown in Fig. 7(d). Compared to the varying window size TF spectra in Fig. 1, our method yields a more focused and accurate TF spectrum [as shown in Fig. 7(c)], effectively tracking the component's IF variations as demonstrated in Fig. 7(d).

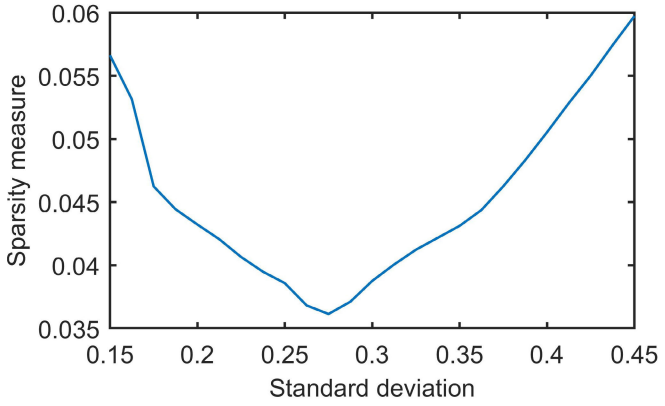

Fig. 4. Sparsity measure of FSST4 versus Gaussian window's standard deviation for long window choosing.

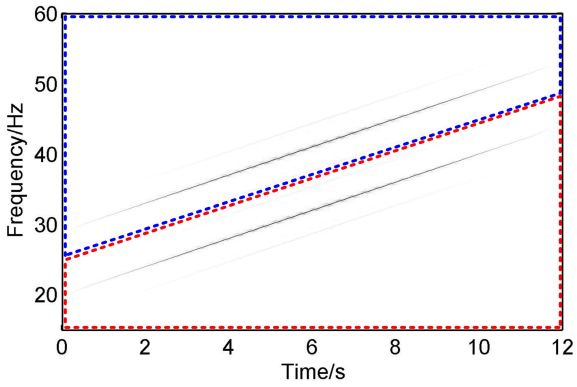

Fig. 5. FSST4-based TF spectra of the synthetic MCS with two slanted FM components ($\sigma = 0.275$).

Furthermore, we add some white noise to the synthetic MCS (SNR = 4.4 dB). The corresponding TF spectra of the proposed method are shown in Fig. 7(e). Although the TF spectra cannot precisely track the frequency variation, it still provides a readable TF spectrum to show the periodic frequency fluctuation.

To quantitively compare different TF spectrum's TF concentration, we show the sparsity measures for different TF analyzing methods (STFT and FSST4) in analyzing the noisy-free synthetic MCS in Table I. The proposed method has the smallest measure, which proves that the proposed TF analyzing method can provide a TF spectrum with a high TF concentration.

B. Oilfield Data Example

Cycle thin-interbeds are one typical geological structure in seismic exploration. The layer thickness cannot be quantitively

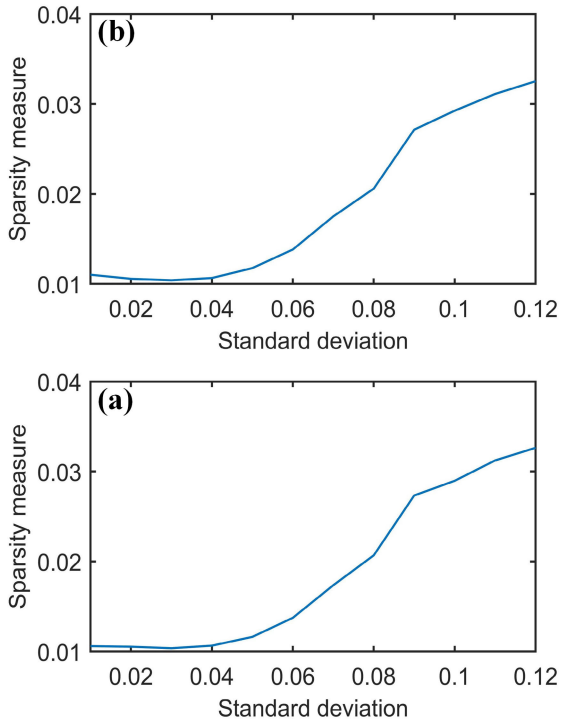

Fig. 6. Sparsity measure of FSST4 versus Gaussian window's standard deviation for small window length choosing. (a) Reconstructed component 1. (b) Reconstructed component 2.

TABLE I

SPARSITY MEASURES FOR DIFFERENT TF METHODS IN ANALYZING THE SYNTHETIC MCS IN FIG. 3

TF method	STFT ($\sigma = 0.275$)	STFT ($\sigma = 0.15$)	STFT ($\sigma = 0.03$)	
Sparsity measure	0.4360	0.5287	0.9387	
TF method	FSST4 ($\sigma = 0.275$)	FSST4 ($\sigma = 0.15$)	FSST4 ($\sigma = 0.03$)	Proposed
Sparsity measure	0.0352	0.0568	0.2237	0.0019

estimated from the seismic dataset because the seismic wavelength is much bigger than the layer's thickness. However, a cycle of thin-interbeds with decreasing thickness will cause its seismic response to have a TF spectrum with an obvious increasing frequency feature, while a cycle thin-interbeds with increasing thickness will cause its seismic response to have a TF spectrum with a noticeable decreasing frequency feature. Therefore, the increasing frequency feature in the TF plane can be used to identify thin interbeds with gradually thinning layers. In contrast, the decreasing frequency feature in the TF plane can be used to identify thin interbeds with gradually thicker layers. The TF spectrum with high TF resolution can be used to track frequency variation to further reflect the layer's thickness variation with depth qualitatively [61].

This real field dataset consists of 1200 traces with a sampling interval of 1 ms and 401 sampling points per trace [Fig. 8(a)]. We only focus on one trace (trace 76) near well A to demonstrate the proposed method's ability to track frequency variation, which can be used to reflect the layer's thickness variation with depth in the cycle thin-interbeds [61]. The waveform of this trace is shown in Fig. 8(b), and the

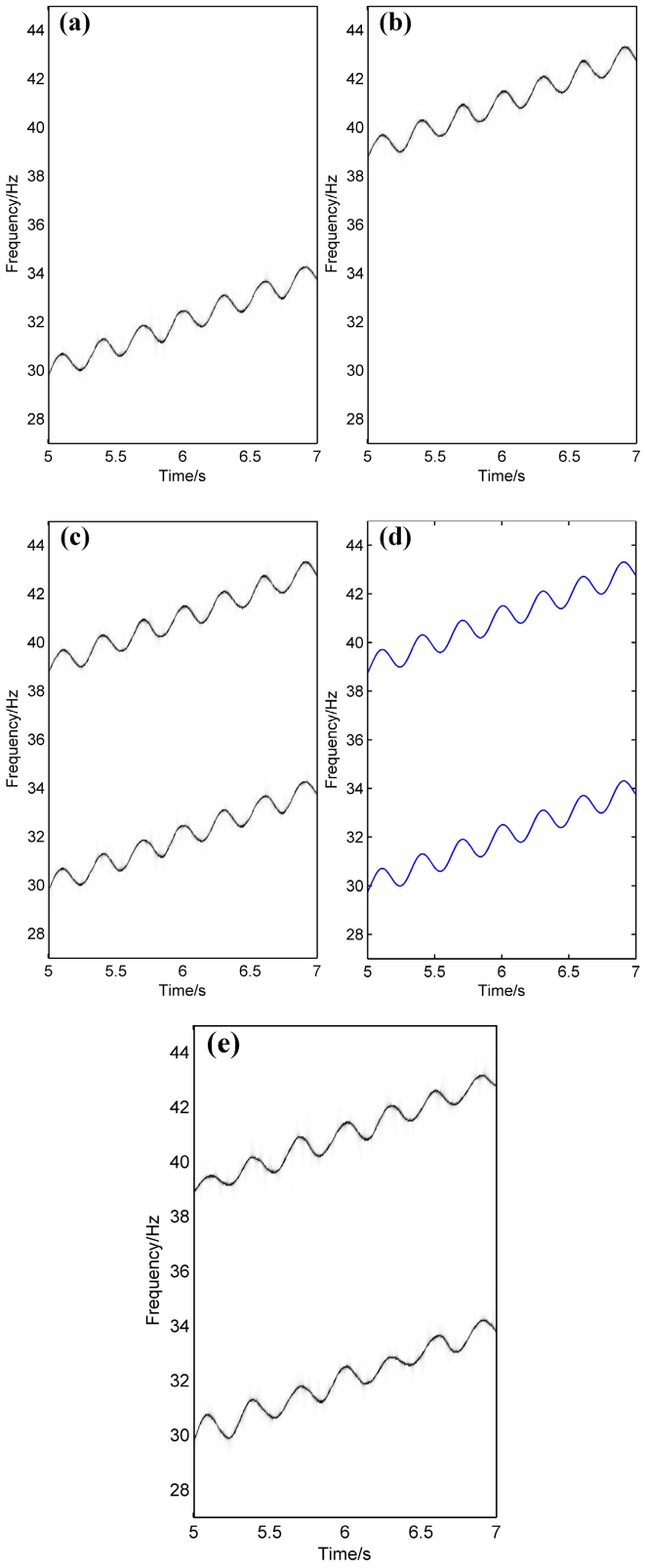

Fig. 7. TF spectra generated by the proposed method for the synthetic MCS with two components. The zoomed TF spectrum by applying the proposed method to (a) reconstructed component 1 and (b) reconstructed component 2. (c) Zoomed TF spectrum of the final TF representation. (d) Ideal IFs of two components in the synthetic MCS (blue curves). (e) Zoomed TF spectrum by the proposed method for the noisy situation (SNR = 4.4 dB).

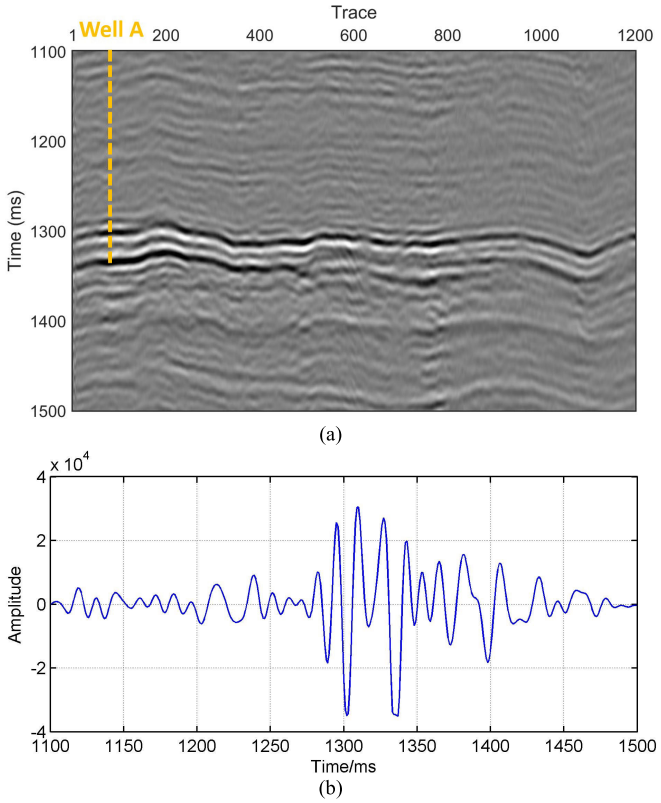

Fig. 8. Real field dataset. (a) 2-D field dataset and the focused well's location. (b) Waveform of the 76th trace.

target reflections are between 1290 and 1340 ms. Because the seismic wavelength is much bigger than the thickness of the targeted layers, it is impossible to estimate their thickness variation quantitatively. The TF spectrum with high TF resolution can be used to estimate the thickness variation qualitatively.

An FSST4 with a long Gaussian window ($\sigma = 0.015$) is applied to this trace to generate one TF spectrum, and the zoomed TF part related to the target area is shown in Fig. 9(a). In addition, the FSST4 with a middle Gaussian window ($\sigma = 0.010$) is applied and the zoomed TF spectrum is shown in Fig. 9(b). Furthermore, the FSST4 with a short Gaussian window ($\sigma = 0.005$) is applied and the zoomed TF spectrum is shown in Fig. 9(c). Although the FSST4 can have a good ability to depict the TF characteristic, these three FSST4s cannot track the frequency variation precisely. The proposed method is applied to this trace. After obtaining the FSST4 with a long window ($\sigma = 0.015$), we reconstruct the signal within the interested part of the TF plane. Then, the FSST4 with a short Gaussian window is applied, and the zoomed TF spectra related to the targeted area are shown in Fig. 9(d). It can be observed that the proposed method can track the frequency variation precisely, while the common FSST4s cannot depict this curve clearly. Our method [Fig. 9(d)] can provide the clearest frequency decreasing than other FSST4s can provide, which means our method has an obvious advantage over other methods in characterizing the layer thickness variation. Furthermore, the TF spectrum provided by the proposed method shows an apparent decreasing frequency [Fig. 9(d)] which indicates the layer thickness was thickening with depth. The

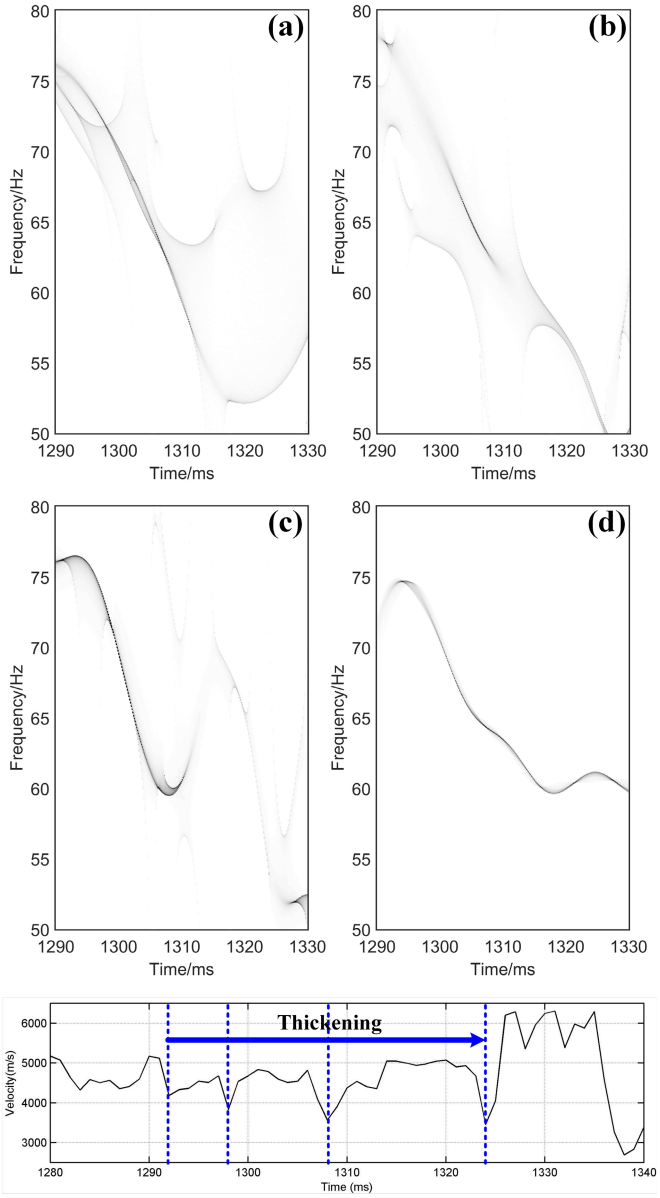

Fig. 9. Enlarged TF spectra for the real seismic signal for oilfield. (a) FSST4 with a long Gaussian window ($\sigma = 0.015$). (b) FSST4 with a middle Gaussian window ($\sigma = 0.010$). (c) FSST4 with a small Gaussian window ($\sigma = 0.005$). (d) Proposed method. (e) Corresponding velocity log near for the focused well.

velocity log for well A shows the layer is thickening near the target area [between 1292 and 1327 ms in Fig. 9(e)], which verifies the decreasing frequency in the TF spectrum provided by the proposed method.

C. HST-Induced Seismic Signal

HST is one of the fastest ways to travel in China. The moving HST will cause the media around the high-speed rail (HSR) to vibrate. The vibrations and seismic waves near the HSR are usually regarded as noise and avoided. In recent years, seismic waves generated by HSTs have received widespread attention and have been used for near-surface structural detection [62], [63], [64], [65], [66], [67], [68], [69], [70], [71]. Here, we used one geophone near Xi'an–Baoji

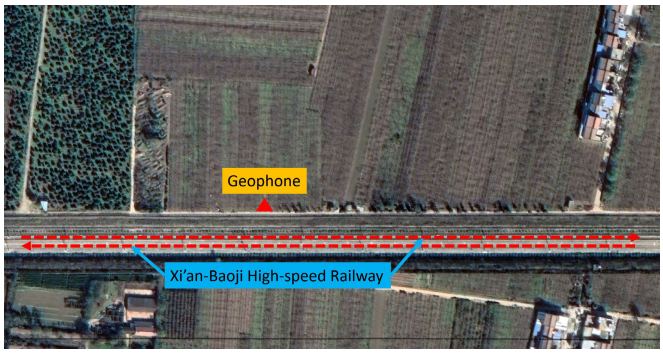

Fig. 10. Positions of geophone and high-speed railway.

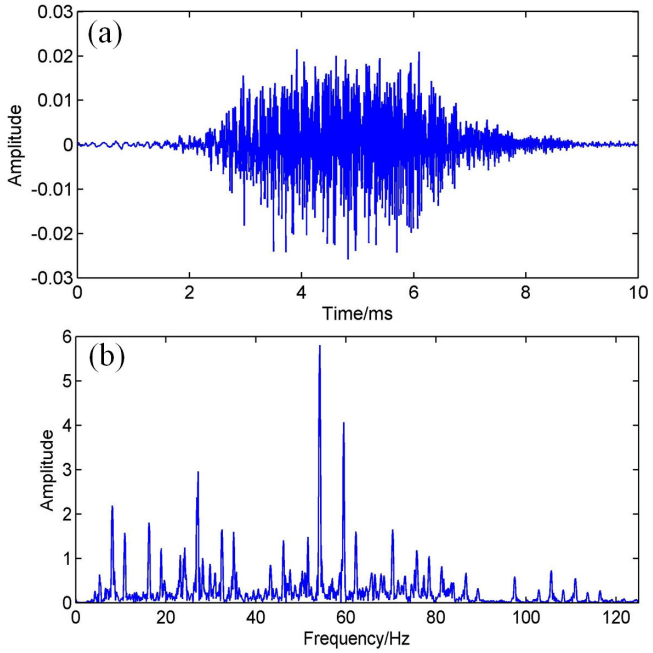

Fig. 11. HST-induced seismic signal received by a geophone near an HSR. (a) Waveform. (b) Amplitude spectrum.

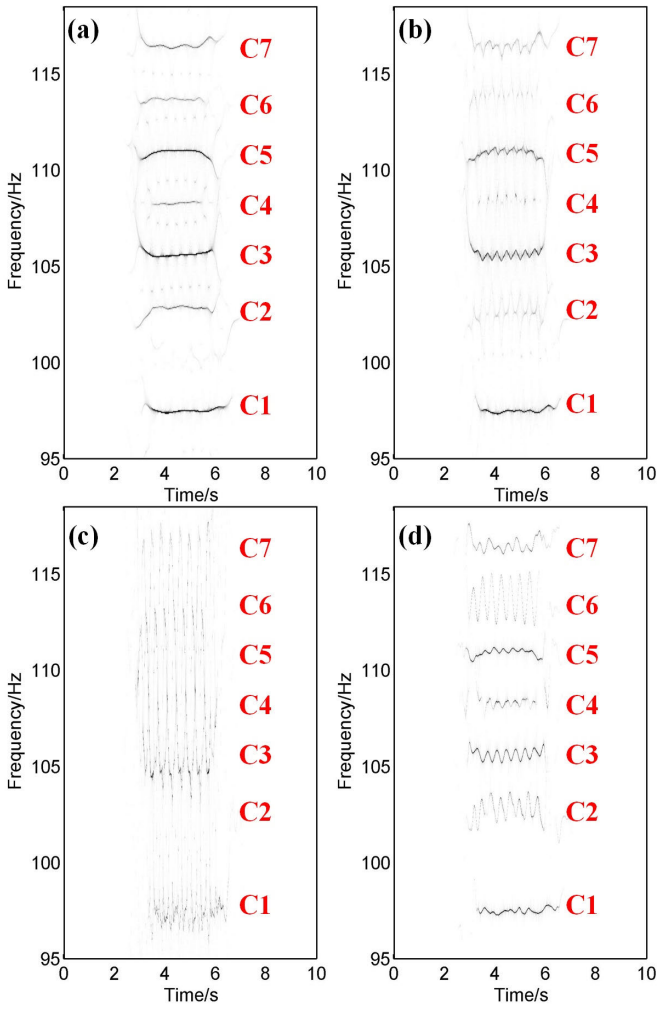

Fig. 12. TF spectra of one HST-induced signal. (a) FSST4 with a long Gaussian window ($\sigma = 0.20$). (b) FSST4 with a middle Gaussian window ($\sigma = 0.125$). (c) FSST4 with a middle Gaussian window ($\sigma = 0.05$). (d) Proposed method.

HSR to receive the seismic signal caused by one HST we focused on, and the positions of the geophone and HSR are shown in Fig. 10. Xi'an Railway Bureau of China, which is the administrative department of this HSR, provided some information about this HST. The operating speed of this HST is 242 km/h (67.22 m/s), and the coach number and length are 8 and 25 m.

According to the recorded HST passing time, we cut the seismic signal induced by this HST and show its waveform and amplitude spectrum in Fig. 11(a) and (b). It can be observed that the spectrum differs from the common exploration signal's amplitude spectrum, which has a continuous and broadband characteristic. The spectrum in Fig. 11(b) also implies that this signal can be treated as an MCS. Therefore, the FSSTN can be utilized to extract this signal's TF characteristics. We use FSST4 with three different length windows and show parts of TF spectra in Fig. 12(a)–(c), respectively. The FSST4 with a long window [Fig. 12(a)] can provide a TF spectrum with a very highly concentrated TF spectrum. Seven main components (from $C1$ to $C7$) can be observed in Fig. 12(a). However, the frequency's variation with time is smoothed in Fig. 12(a). That is to say, long window FSST4 has a low time resolution. On the contrary, the FSST4s with a middle and short window [Fig. 12(b) and (c)] have a good time resolution but suffer from interference between the neighboring components. Therefore, seven components cannot be fully observed in Fig. 12(b) and (c), which means the FSST4 with a short window does not have enough frequency resolution to distinguish seven components.

The proposed method can cascade a long window FSST4 and some short window FSST4s, which can obtain a better balance between time resolution and frequency resolution. The TF spectrum provided by the proposed method is shown in Fig. 12(d). Seven components can be easily observed. Furthermore, for each component's TF spectrum, the frequency's variation with time can be characterized precisely. To further show the TF feature of each component, the TF spectra of component $C3$ are zoomed and shown in Fig. 13. Only the proposed method can provide a concentrated TF spectrum with high time resolution [Fig. 13(d)]. Although FSST4 with a middle Gaussian window [Fig. 13(b)] and a small Gaussian

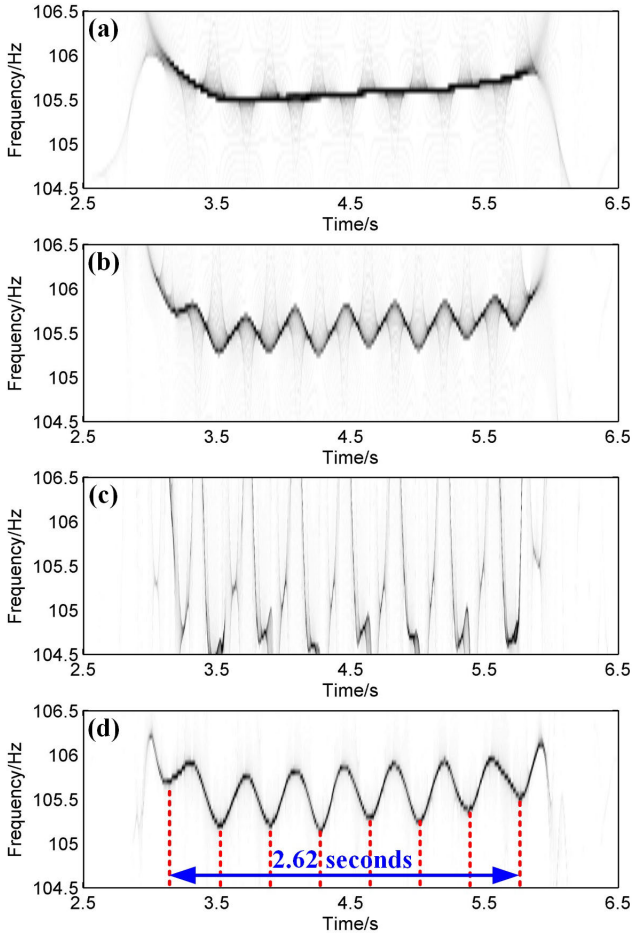

Fig. 13. Zoomed TF spectra of one HST-induced signal. (a) FSST4 with a long Gaussian window ($\sigma = 0.20$). (b) FSST4 with a middle Gaussian window ($\sigma = 0.125$). (c) FSST4 with a small Gaussian window ($\sigma = 0.05$). (d) Proposed method.

window [Fig. 13(c)] can show periodic characteristics of the frequency, the proposed method [Fig. 13(d)] could provide a very concentrated TF spectrum that can be used to recover the periodic characteristic clearly. Furthermore, the frequency variation with time in Fig. 13(d) is periodic, and seven cycles are 2.62 s. Therefore, one cycle time is about 0.374 s.

Compared with the fixed-point seismic source used in traditional seismic exploration, the running HST is a complex moving seismic source. When the HST passes one point in the railway, the load function for this point is one periodic function with eight cycles because the HST we focused on has eight coaches with the same structures [68]. Therefore, it would stimulate a periodic signal with a 0.372-s cycle predicted by the ratio between coach length (25 m) and HST speed (67.22 m/s). The cycle time of the proposed method's TF spectra [Fig. 13(d)] is almost equal to the periodicity caused by the HST. Therefore, our method can provide a high-precision TF spectrum which can reflect the detailed frequency variation with time.

IV. Conclusion

To obtain the TF spectrum with better time resolution and frequency resolution simultaneously, this study proposes a cascaded high-order SST. The proposed transform first uses one high-order FSST with a long window to decompose a signal into several components. Then, the short window high-order FSST applies to each component to obtain a TF representation with high-frequency resolution. The high-order FSST of each component is summed to generate a TF representation with high precision. One synthetic MCS data example has shown the proposed transform's ability to track small frequency fluctuation with time compared with the commonly used high-order FSST. The field data example about layer thickness variation characterization shows that the proposed transform can characterize the tiny frequency variation, which can be used to reflect the layer thickness variation. Finally, the real HST-induced seismic signal data example demonstrates the proposed method's advantages in reflecting the cyclic fluctuation caused by the HST with the same coach structure.

TF analysis has been widely used in seismic data processing and interpretation. Although only two applications have been shown, the proposed method may have potential in low-frequency shadow detection, tiny geologic structure identification, and random noise attenuation. However, the computational cost of the proposed method is higher than the commonly used high-order FSST because multiple high-order FSSTs are involved. Furthermore, like other SSTs, the proposed method works well for a MCS, but it cannot deal with the signal whose components intersect each other in the TF plane because each component cannot be easily separated by the long window TF method.

References

[1] G. Partyka, J. Gridley, and J. Lopez, "Interpretational applications of spectral decomposition in reservoir characterization," *Lead. Edge*, vol. 18, no. 3, pp. 353–360, Mar. 1999.

[2] S. Sinha, P. S. Routh, P. D. Anno, and J. P. Castagna, "Spectral decomposition of seismic data with continuous-wavelet transform," *Geophysics*, vol. 70, no. 6, pp. 19–25, Nov. 2005.

[3] Y. Wang, "Seismic time-frequency spectral decomposition by matching pursuit," *Geophysics*, vol. 72, no. 1, pp. 13–20, Jan. 2007.

[4] Z.-L. Huang, J. Zhang, T.-H. Zhao, and Y. Sun, "Synchrosqueezing S-transform and its application in seismic spectral decomposition," *IEEE Trans. Geosci. Remote Sens.*, vol. 54, no. 2, pp. 817–825, Feb. 2016.

[5] Z. Zhenyu, Z. Wei, and S. Liang, "Spectrum decomposition technology based on physical wavelet transform and its application," *SEG Tech. Program Expanded Abstr.*, vol. 28, no. 1, pp. 1910–1914, 2009.

[6] P. Steeghs and G. Drijkoningen, "Seismic sequence analysis and attribute extraction using quadratic time-frequency representations," *Geophysics*, vol. 66, no. 6, pp. 1947–1959, Nov. 2001.

[7] J. Gao, X. Dong, W.-B. Wang, Y. Li, and C. Pan, "Instantaneous parameters extraction via wavelet transform," *IEEE Trans. Geosci. Remote Sens.*, vol. 37, no. 2, pp. 867–870, Mar. 1999.

[8] S. Sinha, P. Routh, and P. Anno, "Instantaneous spectral attributes using scales in continuous-wavelet transform," *Geophysics*, vol. 74, no. 2, pp. 137–142, Mar. 2009.

[9] Y. Yang, J. Gao, Z. Wang, and Z. Li, "Seismic absorption qualitative indicator via sparse group-lasso-based time-frequency representation," *IEEE Geosci. Remote Sens. Lett.*, vol. 18, no. 9, pp. 1680–1684, Sep. 2021.

[10] X. Wang, J. Gao, W. Chen, W. Zhao, X. Jiang, and Z. Zhu, "Seismic attenuation qualitative characterizing method based on adaptive optimal-kernel time-frequency representation," *J. Appl. Geophysics*, vol. 89, pp. 125–133, Feb. 2013.

[11] J. P. Castagna, S. Sun, and R. W. Siegfried, "Instantaneous spectral analysis: Detection of low-frequency shadows associated with hydrocarbons," *Lead. Edge*, vol. 22, no. 2, pp. 120–127, Feb. 2003.

[12] X. W. Wang, K. Q. Yang, L. H. Zhou, J. Wang, H. Liu, and Y. M. Li, "Methods of calculating coherence cube on the basis of wavelet transform," *Chin. J. Geophys.-Chin. Ed.*, vol. 45, no. 6, p. 847, Nov. 2002.

[13] C. Duan, J. Ai, and Z. Ye, "The application of wavelet transform coherency algorithm in seismic data interpretation," *Prog. Geophys.*, vol. 28, no. 1, pp. 434–438, 2013.

[14] D. Gabor, "Theory of communication. Part 1: The analysis of information," *J. Inst. Electr. Eng. III, Radio Commun. Eng.*, vol. 93, no. 26, pp. 429–441, Nov. 1946.

[15] P. Goupillaud, A. Grossmann, and J. Morlet, "Cycle-octave and related transforms in seismic signal analysis," *Geoexploration*, vol. 23, no. 1, pp. 85–102, Oct. 1984.

[16] A. Grossmann and J. Morlet, "Decomposition of Hardy functions into square integrable wavelets of constant shape," *SIAM J. Math. Anal.*, vol. 15, no. 4, pp. 723–736, Jul. 1984.

[17] R. G. Stockwell, L. Mansinha, and R. P. Lowe, "Localization of the complex spectrum: The S transform," *IEEE Trans. Signal Process.*, vol. 44, no. 4, pp. 998–1001, Apr. 1996.

[18] S. Qian, *Introduction to Time-Frequency and Wavelet Transforms*. Upper Saddle River, NJ, USA: Prentice-Hall, 2002.

[19] E. P. Wigner, "On the quantum correction for thermodynamic equilibrium," in *Part I: Physical Chemistry. Part II: Solid State Physics*. Berlin, Germany: Springer, 1997, pp. 110–120.

[20] L. Cohen, "Time frequency-distributions—A review," *Proc. IEEE*, vol. 77, no. 7, pp. 941–981, Jul. 1989.

[21] F. Auger and P. Flandrin, "Improving the readability of time-frequency and time-scale representations by the reassignment method," *IEEE Trans. Signal Process.*, vol. 43, no. 5, pp. 1068–1089, May 1995.

[22] F. Auger et al., "Time-frequency reassignment and synchrosqueezing: An overview," *IEEE Signal Process. Mag.*, vol. 30, no. 6, pp. 32–41, Nov. 2013.

[23] I. Daubechies, J. Lu, and H.-T. Wu, "Synchrosqueezed wavelet transforms: A tool for empirical mode decomposition," 2009, *arXiv:0912.2437*.

[24] T. Oberlin, S. Meignen, and V. Perrier, "The Fourier-based synchrosqueezing transform," in *Proc. IEEE Int. Conf. Acoustics, Speech Signal Processing*, May 2014, pp. 315–319.

[25] S. Paksima, M. Radad, A. R. Kahoo, and M. S. Monfared, "Identification of thin gas reservoir in reflection seismic data by synchrosqueezing S-transform in time-frequency representation," *Arabian J. Geosci.*, vol. 16, no. 6, pp. 1–12, Jun. 2023.

[26] T. Oberlin, S. Meignen, and V. Perrier, "Second-order synchrosqueezing transform or invertible reassignment? Towards ideal time-frequency representations," *IEEE Trans. Signal Process.*, vol. 63, no. 5, pp. 1335–1344, Mar. 2015.

[27] D. Fourer and F. Auger, "Second-order time-reassigned synchrosqueezing transform: Application to draupner wave analysis," in *Proc. 27th Eur. Signal Process. Conf.*, 2019, pp. 1–5.

[28] Q. Wang, J. Gao, and N. Liu, "Second-order synchrosqueezing wave packet transform and its application for characterizing seismic geological structures," *IEEE Geosci. Remote Sens. Lett.*, vol. 17, no. 5, pp. 760–764, May 2020.

[29] T. Oberlin and S. Meignen, "The second-order wavelet synchrosqueezing transform," in *Proc. IEEE Int. Conf. Acoustics, Speech Signal Process.*, May 2017, pp. 3994–3998.

[30] D.-H. Pham and S. Meignen, "High-order synchrosqueezing transform for multicomponent signals analysis—With an application to gravitational-wave signal," *IEEE Trans. Signal Process.*, vol. 65, no. 12, pp. 3168–3178, Jun. 2017.

[31] Y. Hu, X. Tu, and F. Li, "High-order synchrosqueezing wavelet transform and application to planetary gearbox fault diagnosis," *Mech. Syst. Signal Process.*, vol. 131, pp. 126–151, Sep. 2019.

[32] R. Anvari, M. A. N. Siahsar, S. Gholtashi, A. R. Kahoo, and M. Mohammadi, "Seismic random noise attenuation using synchrosqueezed wavelet transform and low-rank signal matrix approximation," *IEEE Trans. Geosci. Remote Sens.*, vol. 55, no. 11, pp. 6574–6581, Nov. 2017.

[33] Z. Liu, Y. Chen, and J. Ma, "Ground roll attenuation by synchrosqueezed curvelet transform," *J. Appl. Geophys.*, vol. 151, pp. 246–262, Apr. 2018.

[34] R. Anvari, M. Mohammadi, A. R. Kahoo, N. Khan, and A. Abdullah, "Random noise attenuation of 2D seismic data based on sparse low-rank estimation of the seismic signal," *Comput. Geosci.*, vol. 135, Nov. 2019, Art. no. 104376.

[35] R. Anvari, A. R. Kahoo, M. Mohammadi, N. A. Khan, and Y. Chen, "Seismic random noise attenuation using sparse low-rank estimation of the signal in the time-frequency domain," *IEEE J. Sel. Topics Appl. Earth Observ. Remote Sens.*, vol. 12, no. 5, pp. 1612–1618, May 2019.

[36] R. Anvari, A. R. Kahoo, M. S. Monfared, M. Mohammadi, R. M. D. Omer, and A. H. Mohammed, "Random noise attenuation in seismic data using Hankel sparse low-rank approximation," *Comput. Geosci.*, vol. 153, Aug. 2021, Art. no. 104802.

[37] P. Wang, J. Gao, and Z. Wang, "Time-frequency analysis of seismic data using synchrosqueezing transform," *IEEE Geosci. Remote Sens. Lett.*, vol. 11, no. 12, pp. 2042–2044, Dec. 2014.

[38] N. Liu, J. Gao, X. Jiang, Z. Zhang, and Q. Wang, "Seismic time-frequency analysis via STFT-based concentration of frequency and time," *IEEE Geosci. Remote Sens. Lett.*, vol. 14, no. 1, pp. 127–131, Jan. 2017.

[39] Q. Wang, J. Gao, N. Liu, and X. Jiang, "High-resolution seismic time-frequency analysis using the synchrosqueezing generalized S-transform," *IEEE Geosci. Remote Sens. Lett.*, vol. 15, no. 3, pp. 374–378, Mar. 2018.

[40] Z. Li, J. Gao, and Z. Wang, "A time-synchroextracting transform for the time-frequency analysis of seismic data," *IEEE Geosci. Remote Sens. Lett.*, vol. 17, no. 5, pp. 864–868, May 2020.

[41] Z. Li, J. Gao, Z. Wang, N. Liu, and Y. Yang, "Time-synchroextracting general chirplet transform for seismic time-frequency analysis," *IEEE Trans. Geosci. Remote Sens.*, vol. 58, no. 12, pp. 8626–8636, Dec. 2020.

[42] X. Wang, B. Wang, and W. Chen, "The second-order synchrosqueezing continuous wavelet transform and its application in the high-speed-train induced seismic signal," *IEEE Geosci. Remote Sens. Lett.*, vol. 18, no. 6, pp. 1109–1113, Jun. 2021.

[43] L. Xu, X. Yin, Z. Zong, and K. Li, "Synchrosqueezing matching pursuit time-frequency analysis," *IEEE Geosci. Remote Sens. Lett.*, vol. 18, no. 3, pp. 411–415, Mar. 2021.

[44] Q. Wang, Y. Li, S. Chen, and B. Tang, "Matching demodulation synchrosqueezing S transform and its application in seismic time-frequency analysis," *IEEE Geosci. Remote Sens. Lett.*, vol. 19, pp. 1–5, 2022.

[45] R. Kumar, P. Sumathi, and A. Kumar, "Synchrosqueezing transform-based frequency shifting detection for earthquake-damaged structures," *IEEE Geosci. Remote Sens. Lett.*, vol. 14, no. 8, pp. 1393–1397, Aug. 2017.

[46] X. Chen, H. Chen, R. Li, Y. Hu, and Y. Fang, "Multisynchrosqueezing generalized S-transform and its application in tight sandstone gas reservoir identification," *IEEE Geosci. Remote Sens. Lett.*, vol. 19, pp. 1–5, 2022.

[47] G. Zhang et al., "Adaptive time-resampled high-resolution synchrosqueezing transform and its application in seismic data," *IEEE Trans. Geosci. Remote Sens.*, vol. 58, no. 9, pp. 6691–6698, Sep. 2020.

[48] A. Mahdavi, A. R. Kahoo, M. Radad, and M. S. Monfared, "Application of the local maximum synchrosqueezing transform for seismic data," *Digit. Signal Process.*, vol. 110, Mar. 2021, Art. no. 102934.

[49] R. Anvari, A. Hussein Mohammed, and S. Rashidi, "Time-reassigned synchrosqueezing transform and low-frequency shadows associated with gas detection," in *Proc. 4th Int. Conf. Commun. Eng. Comput. Sci.*, 2022, pp. 98–104.

[50] Z. Hu, J. Gao, and N. Liu, "Separation of blended seismic data using the synchrosqueezed curvelet transform," *IEEE Geosci. Remote Sens. Lett.*, vol. 17, no. 4, pp. 711–715, Apr. 2020.

[51] R. H. Herrera, J. B. Tary, M. van der Baan, and D. W. Eaton, "Body wave separation in the time-frequency domain," *IEEE Geosci. Remote Sens. Lett.*, vol. 12, no. 2, pp. 364–368, Feb. 2015.

[52] Y.-J. Xue, A. Pirogova, J.-X. Cao, and X.-J. Wang, "Q-factor estimation by compensation of amplitude spectra in synchrosqueezed wavelet domain," *IEEE Trans. Geosci. Remote Sens.*, vol. 59, no. 3, pp. 2657–2665, Mar. 2021.

[53] Y. Zhao and Y. Su, "Synchrosqueezing phase analysis on micro-Doppler parameters for small UAVs identification with multichannel radar," *IEEE Geosci. Remote Sens. Lett.*, vol. 17, no. 3, pp. 411–415, Mar. 2020.

[54] R. Wang, M. Xiang, B. Wang, and C. Li, "Nonlinear phase estimation and compensation for FMCW ladar based on synchrosqueezing wavelet transform," *IEEE Geosci. Remote Sens. Lett.*, vol. 18, no. 7, pp. 1174–1178, Jul. 2021.

[55] G. Zhang and J. Gao, "Inversion-driven attenuation compensation using synchrosqueezing transform," *IEEE Geosci. Remote Sens. Lett.*, vol. 15, no. 1, pp. 132–136, Jan. 2018.

[56] N. Liu, Z. Li, F. Sun, F. Li, and J. Gao, "Seismic geologic structure characterization using a high-order spectrum-coherence attribute," *Interpretation*, vol. 8, no. 2, pp. 391–401, May 2020.

[57] X. Chen, H. Chen, Y. Fang, and Y. Hu, "High-order synchroextracting time-frequency analysis and its application in seismic hydrocarbon reservoir identification," *IEEE Geosci. Remote Sens. Lett.*, vol. 18, no. 11, pp. 2011–2015, Nov. 2021.

[58] R. Tian, X. Lei, and J. Hu, "Application of time-frequency entropy based on high-order synchrosqueezing transform in reservoir prediction," *Interpretation*, vol. 8, no. 3, pp. T667–T674, Aug. 2020.

[59] L. Staniovic, "A measure of some time-frequency distributions concentration," *Signal Process.*, vol. 8, no. 3, pp. 621–631, 2001.
[60] S. Meignen, D.-H. Pham, and S. McLaughlin, "On demodulation, ridge detection, and synchrosqueezing for multicomponent signals," *IEEE Trans. Signal Process.*, vol. 65, no. 8, pp. 2093–2103, Apr. 2017.
[61] X. Wang, C. Li, and W. Chen, "Seismic thin interbeds analysis based on high-order synchrosqueezing transform," *IEEE Trans. Geosci. Remote Sens.*, vol. 60, 2022, Art. no. 5908611.
[62] W. Xiaokai, W. Baoli, C. Wenchao, and L. Jiaqi, "Using the data from one receiver to estimate running velocity of high-speed train," *Acta Scientiarum Naturalium Universitatis Pekinensis*, vol. 55, no. 5, pp. 798–804, 2019.
[63] W. XiaoKai, C. JianYou, C. WenChao, J. YiRan, B. TieZhao, and N. JieYuan, "Sparse modeling of seismic signals produced by high-speed trains," *Chin. J. Geophys.-Chin. Ed.*, vol. 62, no. 6, pp. 2336–2343, 2019.
[64] X. Wang, W. Chen, J. Wen, J. Ning, and J. Li, "The applications of synchrosqueezing time-frequency analysis in high-speed train induced seismic data processing," *Chin. J. Geophys.-Chin. Ed.*, vol. 62, no. 6, pp. 2328–2335, 2019.
[65] Y. Liu, Y. Yue, Y. Li, and Y. Luo, "On the retrievability of seismic waves from high-speed-train-induced vibrations using seismic interferometry," *IEEE Geosci. Remote Sens. Lett.*, vol. 19, pp. 1–5, 2022.
[66] Y. Liu, Y. Yue, Y. Luo, and Y. Li, "Effects of high-speed train traffic characteristics on seismic interferometry," *Geophys. J. Int.*, vol. 227, no. 1, pp. 16–32, May 2021.
[67] Y. Liu, Y. Yue, Y. Luo, and Y. Li, "The seismic broad-band signature of high-speed trains running on viaducts," *Geophys. J. Int.*, vol. 226, no. 2, pp. 884–892, Mar. 2021.
[68] X. Wang, B. Wang, C. Li, W. Chen, and C. Zhao, "High-speed train speed estimation via one geophone near an high-speed railway," in *Proc. 1st Int. Meeting Appl. Geosci. Energy*, 2021, pp. 3230–3234.
[69] J. Luo, X. Wang, and W. Chen, "Subsurface elastic parameter reconstruction based on seismic data from the high-speed trains using full waveform inversion," *IEEE Trans. Geosci. Remote Sens.*, vol. 60, 2022, Art. no. 4508008.
[70] J. Shao, Y. Wang, and L. Chen, "Near-surface characterization using high-speed train seismic data recorded by a distributed acoustic sensing array," *IEEE Trans. Geosci. Remote Sens.*, vol. 60, 2022, Art. no. 5912911.
[71] J. Luo, X. Wang, and W. Chen, "Imaging the subsurface with the high-speed train seismic data-based elastic reverse time migration," *IEEE Trans. Geosci. Remote Sens.*, vol. 61, 2023, Art. no. 4505409.

Xiaokai Wang (Member, IEEE) received the B.S. degree in information engineering and the Ph.D. degree in communication engineering from Xi'an Jiaotong University (XJTU), Xi'an, China, in 2006 and 2012, respectively.

He was a Post-Doctoral Fellow with the Institute of Geology and Geophysics, Chinese Academy of Sciences, Beijing, China, from 2012 to 2014. He joined the Department of Computational Geophysics, XJTU, in 2015. He was a Visiting Scholar of Bureau of Economic Geology, The University of Texas at Austin, Austin, TX, USA, from 2016 to 2017. His research interests include seismic attributes extraction, time–frequency (TF) analysis, and high-speed rail (HSR) seismology.

Dawei Liu received the bachelors' degree in communication engineering from Chang'an University, Xi'an, China, in 2013, the master's degree in electronic and communication engineering from Xi'an Jiaotong University (XJTU), Xi'an, in 2018, and the Ph.D. degree from the School of Information and Communication Engineering in 2022.

He is currently a Post-Doctoral Scholar with Purdue University. His research interests include tensor decomposition, deep learning, and time-frequency analysis and their applications in the seismic data processing.

Dr. Lin is a reviewer of IEEE TRANSACTIONS ON GEOSCIENCE AND REMOTE SENSING, GEOPHYSICS, ACTA GEOPHYSICA, PETROLEUM SCIENCE, etc.

Wenchao Chen received the B.S. and M.S. degrees in seismic exploration and information technology from Chang'an University, Xi'an, China, in 1993 and 1996, respectively, and the Ph.D. degree in electromagnetic field and microwave technology from Xi'an Jiaotong University, Xi'an, in 2000.

From 2000 to 2002, he was a Post-Doctoral Fellow with the Department of Computation Science, Northwestern Polytechnical University, Xi'an. Since 2002, he has been with Xi'an Jiaotong University, where he is currently a Professor. His research interests include high-speed rail (HSR) seismology, seismic and GPR signal processing, blind signal processing, and sparse representation.

Dr. Chen is a member of SEG and the Chinese Geophysical Society. He is also a referee for several journals, including the IEEE JOURNAL OF SELECTED TOPICS IN APPLIED EARTH OBSERVATIONS AND REMOTE SENSING, IEEE TRANSACTIONS ON GEOSCIENCE AND REMOTE SENSING, *Geophysics*, *Interpretation,* and *Journal of Applied Geophysics*.

Chun Li received the B.S. degree in safety engineering from the Xi'an University of Science and Technology, Xi'an, China, in 2019. He is currently pursuing the master's degree with the School of Information and Communication Engineering, Xi'an Jiaotong University (XJTU), Xi'an.

His research interests include time–frequency (TF) analysis and seismic signal processing.